ARTICLE

Enhanced Conversion Efficiency in Dye-Sensitized Solar Cells Based on Hydrothermally Synthesized TiO_2—MWCNT Nanocomposites

Subas Muduli,[†] Wonjoo Lee,[‡] Vivek Dhas,[†] Sarfraj Mujawar,[†] Megha Dubey,[†] K. Vijayamohanan,[†] Sung-Hwan Han,[‡] and Satishchandra Ogale*,[†]

Physical and Materials Chemistry Division, National Chemical Laboratory, Dr. Homi Bhabha Road, Pashan, Pune 411 008, India, and Department of Chemistry, Hanyang University, Haengdang-dong 17, Sungdong-ku, Seoul 133-791, Korea

ABSTRACT A 50% enhancement in the conversion efficiency (4.9—7.37%) is realized in dye-sensitized solar cells using hydrothermally synthesized TiO_2—multiwalled carbon nanotube (MWCNT) nanocomposites as compared to hydrothermally synthesized TiO_2 without MWCNT and Degussa P25. Several characterizations have been employed to reveal the nature of the modification imparted to the MWCNTs under hydrothermal processing conditions and the resulting TiO_2—MWCNT conjugation through —COOH groups. Efficient charge transfer in the nanocomposite and efficient electron transport by MWCNT (significantly higher incident-photon-to-current conversion efficiency) are suggested to be the possible reasons for the enhancement.

KEYWORDS: hydrothermal • dye-sensitized solar cells • carbon nanotubes • hybrid composite • charge transfer

INTRODUCTION

Dye-sensitized solar cells (DSSCs) represent a key class of cell architecture that has emerged as a promising candidate for the development of next-generation solar cells (1, 2). With suitable engineering and optimization of the nanostructure for its optical, electrical, and morphological properties, its porosity, light-harvesting characteristics, etc., these cells have been shown to deliver fairly high power efficiencies (1, 3, 4). This, compounded with the low materials/processing cost and the ease of manufacturing, has led to significant efforts in recent years to improve their performance. The efficiency of collection of the photogenerated carriers at the two electrodes is a critical factor in the device performance. It is determined by the competition between the electron transport to the anode and the electron transfer to I^{3-} ions in the electrolyte. In order to improve the efficiency of DSSCs, various ideas have been pursued. These include deposition of a thin tunneling barrier layer on the substrate (5—7), incorporation of an ultrathin layer of insulating oxide on the surface of the mesoporous film of TiO_2 (8), concurrent use of different dyes for cosensitization (9), post-treatment using a $TiCl_4$ precursor (10, 11), etc. A bilayer structure involving an additional light-harvesting layer is also employed widely because it confines the incident light within the electrode, enhancing the photocurrent density (12—14). One of the major bottlenecks that often limit the performance of these solar cells is the efficiency of electron transport across the nanoparticulate network because the interparticle interface scattering encountered during the electron transit effectively enhances electron recombination before their efficient collection at the electrode surface. It is to reduce such undesirable effects dramatically that suggestions have been made and experimented upon using extended charge-carrier pathways such as nanotubes, nanorods, flowers, etc., as integrated elements of the cell architecture (15, 16). Either such geometric forms can be added in a simple physical mixture with nanoparticulates that eventually get sintered together by adequate thermal processing or nanocomposites of extended and particular structures can be preformed and used for making the cells. The latter one is an attractive proposition because it gives avenues to engineer the structural and electrical characteristics of the interfaces during the synthesis protocol itself. Several attempts have been made using both strategies, and enhancements in efficiencies have been realized (3, 4). One category of an extended quasi-1D material that has attracted considerable attention in this regard is carbon nanotubes (CNTs) for its good and controllable electrical characteristics and compatible band line-ups with metal oxide nanosystems of interest such as TiO_2, ZnO, etc. (17—27).

Chen et al. synthesized CNT—TiO_2 nanocomposites by hydrolysis wherein the formation of TiO_2 and its compounding with TiO_2 happened almost simultaneously with interface formation via polar oxygenated groups, though these

* Corresponding author. Tel: +91-20-25902260. Fax: +91-20-2590-2636. E-mail: sb.ogale@ncl.res.in.
Received for review June 08, 2009 and accepted August 17, 2009
[†] National Chemical Laboratory.
[‡] Hanyang University.
DOI: 10.1021/am900396m

Published on Web 08/28/2009

authors did not report on photovoltaic or photocatalytic measurements (28). Lee et al. used nanocomposites of preprocessed multiwalled CNTs (MWCNTs) with carboxylic acid groups and TiO_2 nanoparticles (NPs) synthesized via a sol–gel process for DSSCs and obtained a conversion efficiency of 4.97% with a 0.1 wt % CNT (24). Kamat and coworkers have done significant work on nanocomposites of single-walled CNTs (SWCNTs) with TiO_2 in the context of photovoltaic and photocatalytic applications. They have demonstrated efficiency enhancements and have also elucidated the attendant mechanisms of photoinduced charge separation and carrier transport to the collecting electrodes (17–19). Yen et al. used a modified acid-catalyzed sol–gel method to synthesize MWCNT–TiO_2 nanocomposites and examined them for DSSC performance. They emphasized the importance of optimum CNT loading to realize an efficiency of 4.62% (21). Lee et al. have also realized a DSSC efficiency of 5.02% using MWCNT–TiO_2 nanocomposites, which projects improvement by ~50% over the case without MWCNT (23). More recently, Sawatsuk et al. have shown improvement in the efficiency of DSSC by almost 60% by a simple mixing process (29).

In the present work, we have employed a hydrothermal route to synthesize TiO_2–MWCNT nanocomposites and have realized a significant enhancement in the power conversion efficiency of DSSCs (7.4%). Using various characterizations, we analyze the possible origin of the observed effects. It is useful to mention here that the hydrothermal process, in which the chemical reaction could take place under autogenerated pressure upon heating, is efficient to achieve a crystalline phase at relatively low temperatures (30, 31). It is suggested that the high pressure can render denser materials with fewer defects and good crystallinity as compared to other milder routes.

EXPERIMENTAL SECTION

Materials. Chemical agents were purchased from Aldrich Co., and $RuL_2(NCS)_2/(TBA)_2$ (N719; L = 2,2′-bipyridine-4,4′-dicarboxylic acid and TBA = tetrabutylammonium) was purchased from Solaronix Co. and used as received. MWCNTs (95% purity) having diameters of 20–40 nm and lengths of 5–15 μm were obtained from Monald Tech (India). A fluorine-doped SnO_2 (FTO) electrode (sheet resistance = 8 ohm/□; transmittance = 77% in the visible range) was obtained from Pilkington TEC Glass. For the preparation of reference DSSCs, commercial TiO_2 was obtained from Degussa (P25). High-purity water (Milli-Q, Millipore) was used for all experiments. The FTO electrodes were washed with acetone, ethanol, and deionized (18.2 MΩ · cm) water in an ultrasonication bath for 15 min with a final wash in isopropyl alcohol.

Preparation of a TiO_2-MWCNT Nanocomposite. The TiO_2–MWCNT nanocomposite was prepared by using a hydrothermal method. Titanium isopropoxide (2 mL) was hydrolyzed by adding a sufficient amount of deionized water, and then a few milligrams of MWCNT was added to the above solution, followed by sonication for 5 min. The solution was then transferred to a Teflon-lined autoclave vessel along with 3 mL of H_2SO_4 (1 M). This autoclave vessel was kept at 175 °C for 24 h. The resulting product was washed thoroughly with deionized water and dried at 50 °C in a dust-proof environment to produce a grayish powder of TiO_2–MWCNT nanocomposite.

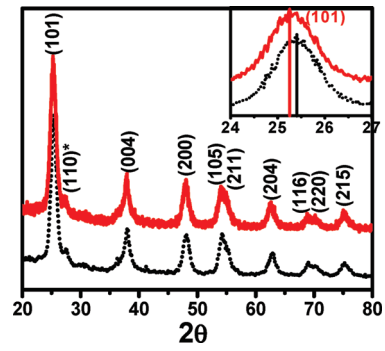

FIGURE 1. XRD patterns of TiO_2 (short dotted line) and TiO_2–MWCNT (solid line) nanocomposite.

Characterization. Various techniques such as X-ray diffraction (XRD; Philips X'Pert PRO), Raman spectroscopy (Horiba Jobin Yvon LabRAM HR System), transmission electron microscopy (TEM), field-emission scanning electron microscopy (FE-SEM; Hitachi S-4200), and FT-IR spectroscopy (Perkin-Elmer Spectra One) were used to characterize the samples. The formation of TiO_2–MWCNT nanocomposite films was carried out by the doctor blade method, and the films were then annealed at 450 °C for 30 min. The thickness of TiO_2–MWCNT nanocomposite films was ~12 μm. For sensitization, the TiO_2–MWCNT nanocomposite films were impregnated with 0.5 mM N719 dye in ethanol for 24 h at room temperature. The sensitizer-coated TiO_2 films were washed with ethanol.

Measurements. The J–V characteristics were measured by irradiation with 100 mW/cm^2 (450 W xenon lamp, Oriel Instruments), 1 sun AM 1.5, simulated sunlight as a solar simulator in the presence of a water filter. The current was measured using a Kiethley 2400 source. The electrolytes were used with 0.6 M 1-hexyl-2,3-dimethylimidazolium iodide, 0.1 M LiI, 0.05 M I_2, and 0.5 M 4-*tert*-butylpyridine in methoxyacetonitrile. Measurements of the incident-photon-to-current conversion efficiency (IPCE) were carried out without bias illumination with respect to a calibrated Melles-Friot silicon diode. IPCE was measured by changing the excitation wavelength (photon-counting spectrometer, ISS Inc., and Kiethley 2400 source meter).

RESULTS AND DISCUSSION

Crystal Structure of a TiO_2–MWCNT Nanocomposite. Figure 1 compares the XRD patterns for TiO_2 NPs and a TiO_2–MWCNT nanocomposite synthesized by a hydrothermal route. The peaks in Figure 1 at 25.28 (101), 37.80 (004), 48.18 (200), and 54.09 (105) (PCPDFWIN # 211 272) clearly represent the anatase TiO_2 phase with a tiny amount of the (110) rutile phase contribution (PCPDFWIN # 211 276) observed at 27.22. The 100% XRD peak intensity for CNT (PCPDFWIN # 411 487) is expected at 26.38 (002), which is not apparent because of its small amount in the composition of TiO_2–MWCNTs [as well as its low Z as compared to the dominant TiO_2 (high Z)], but the same can be clearly elucidated by Raman analysis as discussed later. As indicated in the inset, we did see a tiny but definitive shift in the XRD peak positions, possibly suggesting strain (and particle size) effects originating in the integration between the TiO_2 NPs and the MWCNT surface. It also suggests that our process leads to real integration across the interface rather than the formation of a mere mixture, as we bring out more conclusively via Raman and FT-IR analysis.

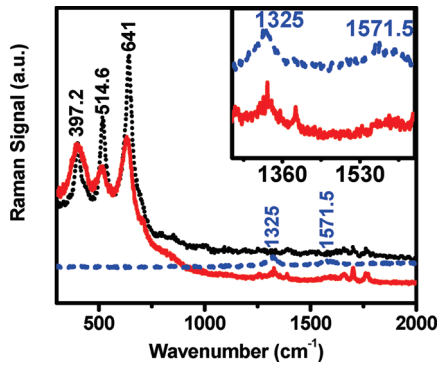

FIGURE 2. Raman spectra for MWCNTs (dashed line), TiO_2 (short dotted line), and a TiO_2–MWCNT nanocomposite (solid line). The inset shows a specific region of the data on an expanded scale.

The Raman spectra for TiO_2 and TiO_2–MWCNT nanocomposite powders are shown in Figure 2. The Raman spectrum for the case of pure TiO_2 shows clear signatures at about 397.2, 514.6, and 641 cm^{-1}, as expected (32), while for the pure MWCNT case, the Raman features are observed at 1325 and 1571.5 cm^{-1}, as reported (25). As seen from the inset, clear signatures of MWCNTs are also noted in the TiO_2–MWCNT nanocomposite spectrum, along with those for TiO_2 in that spectral region. Interestingly, the main three features (397.2, 514.6, and 641 cm^{-1}) in the Raman spectrum representative of anatase TiO_2 are broadened in the case of the TiO_2–MWCNT nanocomposite sample as compared to the only TiO_2 case. Such a broadening can occur because of strain gradients originating from interface integration or particle size distribution and has been observed in other nanocomposite systems with MWCNT (29, 33). In thin films, it is well-known that strain effects can extend to several nanometers into materials (critical thickness) depending on the lattice misfit. In the present case, one has a molecular substrate on which the TiO_2 NPs are getting chemically anchored. It is difficult to define strain in precise terms in this organic–inorganic complex interface system. However, given the nanoscopic nature of the particles, which leads to a higher concentration of surface atoms and attendant phonon softening, one could expect strain gradients to extend almost over the particle dimension, which in our case is around 8–10 nm. We believe that in addition to strain the Raman line broadening could occur because of the particle size distribution. Indeed, in the present case, because the MWCNT concentration is small, it is possible that, in addition to heterogeneous nucleation on the MWCNT surface, some NPs could grow via homogeneous nucleation and may have a different size distribution. Admittedly, more work will be needed to resolve the precise origin of the broadening.

Morphological Characterization. Figure 3a shows the TEM image of TiO_2 NPs synthesized by the hydrothermal process without incorporation of MWCNT. The mean particle size is about 8–10 nm and the particles are faceted, suggesting good crystallinity, as expected in a hydrothermal process. Figure 3b shows the TEM image of MWCNTs used in the experiment, indicating its dimensions (diameter ~ 20–40 nm and length ~ 5–15 μm). The integration between MWCNT and TiO_2 NPs discussed above can be visualized from the FE-SEM data shown in Figure 3c. A very uniform growth with excellent TiO_2 NPs coverage can be clearly seen. As will be discussed next, the hydrothermal processing environmental surface modifies MWCNTs to enable such growth. We now address the issue of the possible modification imparted by the hydrothermal treatment used to prepare the nanocomposite to examine the possible routes for interface integration of growing TiO_2 NPs on its surface.

FT-IR Spectra. Figure 4A shows the FT-IR data of (a) pristine MWCNTs, (b) TiO_2 NPs, (c) hydrothermally processed MWCNTs, and (d) TiO_2–MWCNT nanocomposites. The bonding between Ti–O is clearly represented in the region near 500 cm^{-1}. It is interesting to note from the black and red arrows in this region that the mean position of the signature shifts from about 520 cm^{-1} in the TiO_2 case to about 612 cm^{-1} for the TiO_2–MWCNT composite. This can be attributed to different size distributions and possible levels of strains in the two cases. Interestingly, only in the cases of hydrothermally processed samples involving MWCNT (namely, MWCNT and TiO_2–MWCNT) do we note clear signatures centered near 1143 and 1735 cm^{-1}. The signature near 1143 cm^{-1} is in the fingerprint region and, hence, difficult to assign uniquely. However, the occurrence of the signature near 1735 cm^{-1} (see the circled region) with a contribution in the region of around 3400 cm^{-1} (OH stretch, which also overlaps with other contributions) together indicate the presence of a –COOH group only in the hydrothermally processed cases involving MWCNT (35). From Figure 4B, it can be noted that in the TiO_2–MWCNT nanocomposite the same signature appears a bit shifted to 1745 cm^{-1}, suggesting the effect of conjugation of TiO_2 on the modified MWCNT surface. Other characteristic bands including the sharp one near 1380 cm^{-1} are generated because of different mineralizer residues used in the hydrothermal process. In light of this result, we now address the issue of possible modification imparted by the hydrothermal treatment used to prepare the nanocomposite to examine the possible routes for interface integration of growing TiO_2 NPs on its surface.

Because the –OH group on the Ti precursor and the C–O, C═O, and O–C═O groups opened up on the surface of MWCNTs due to hydrothermal treatment, properly integrated nanocomposites can form naturally through some physicochemical actions involving van der Waals force, hydrogen bonding, and other bonding types. For example, the –OH group on the Ti precursor may possibly react with the –OH and –COOH groups on the MWCNT surface in removing H_2O contained in wet fresh composites. Thus, the bonding of the form C–O–Ti or *O*═C–O–Ti might form through the dehydration reaction among the groups on the two materials (28). As indicated in Figure 4B, the shift of the carbonyl group (C═O) from 1735 cm^{-1} (in hydrothermally processed MWCNTs) to 1745 cm^{-1} (in TiO_2–MWCNT nanocomposites) indicates the interaction of the carboxylate

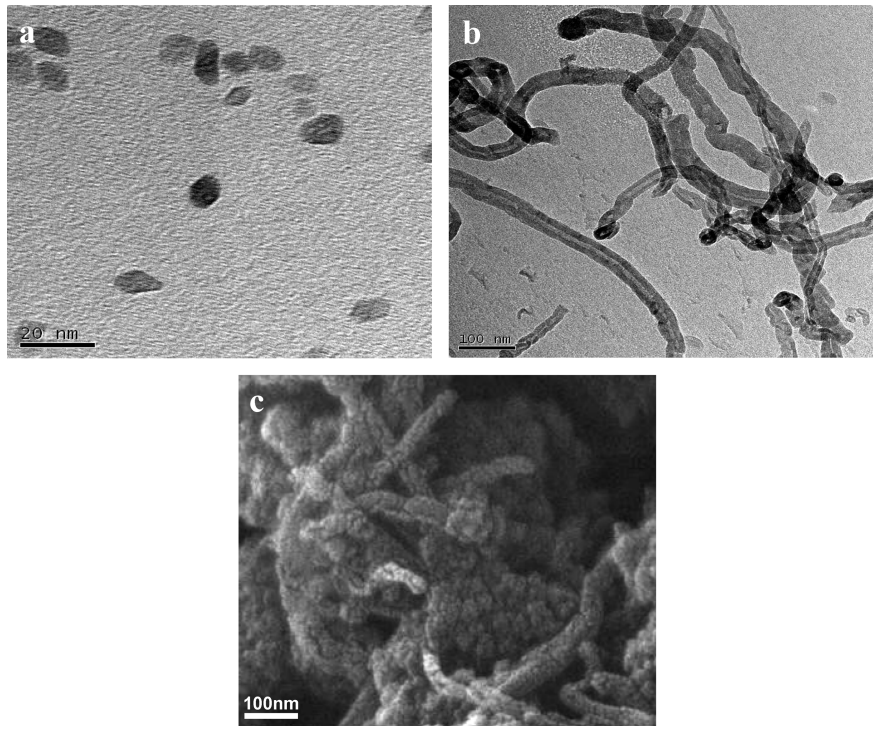

FIGURE 3. TEM images of (a) TiO_2 NPs and (b) MWCNT. (c) FE-SEM data showing integrated growth of TiO_2 on MWCNTs.

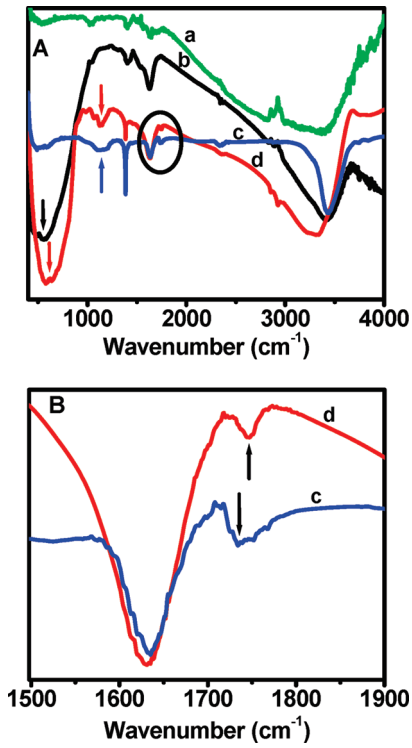

FIGURE 4. FT-IR data for the (a) pristine MWCNTs, (b) TiO_2 NPs, (c) hydrothermally processed MWCNTs, and (d) TiO_2–MWCNT nanocomposites.

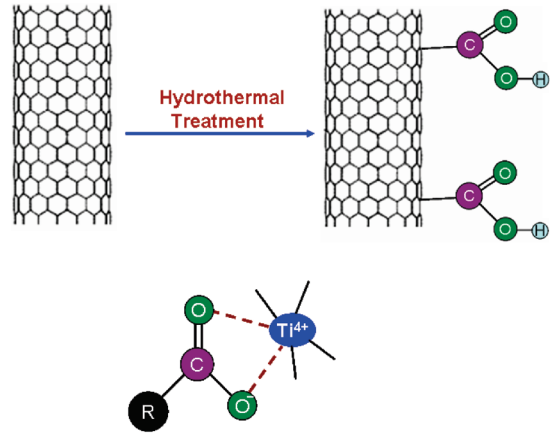

FIGURE 5. Schematic of the functionalization of MWCNTs under hydrothermal treatment and the attachment of functionalized MWCNTs with TiO_2 NPs (R belongs to MWCNTs).

group with the Ti precursor. In Figure 5, we present a schematic of the suggested process.

We evaluated the performance of the TiO_2–MWCNT nanocomposite as an electrode for photovoltaic application by recording the IPCE at different incident wavelengths of light. As a reference cell, commercial TiO_2 films were prepared by P25 (Degussa). Figure 6 shows IPCE spectra as a function of the wavelength for the P25 and TiO_2–MWCNT samples, which was calculated from the equation IPCE (%) $= 1240 J_{SC}/\lambda P_{in}$, where J_{SC} is the short-circuit current density, λ is the wavelength of the incident light, and P_{in} is the power of the incident light. The absolute IPCE for TiO_2–MWCNTs is significantly higher than that for P25 over the entire wavelength region, which is in good agreement with the observed higher short-circuit photocurrent density (J_{sc}), as shown later. Both of these electrodes exhibit an IPCE maximum corresponding to the absorption maximum of the Ru^{II} complex. The IPCE response at all wavelengths is enhanced from ~47% to ~70% as a result of the introduction of MWCNT scaffolds in the mesoscopic TiO_2 film. Factors controlling the IPCE in DSSCs have been discussed in detail by several research groups (18). Suppressing the back electron transfer and improving the electron transport

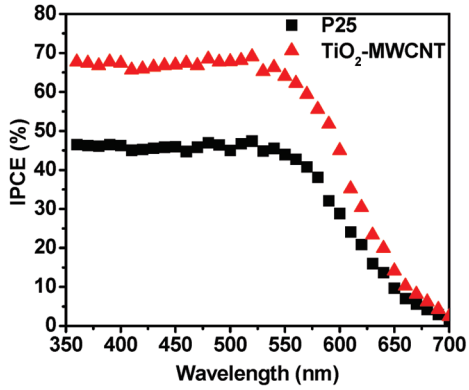

FIGURE 6. IPCE data for TiO_2−MWCNT nanocomposites as compared to the corresponding P25 data.

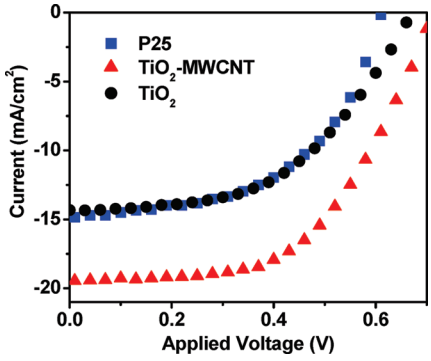

FIGURE 7. $J-V$ characteristics for a TiO_2−MWCNT nanocomposite as compared to the corresponding cases of P25 and hydrothermally synthesized TiO_2 NPs without MWCNT.

Table 1. Performance Parameters of DSSCs Fabricated with P25, Hydrothermally Synthesized TiO_2 NPs without MWCNT, and TiO_2−MWCNT Nanocomposite Powder

name	V_{OC} (V)	J_{SC} (mA/cm^2)	fill factor (FF)	efficiency (η)
Degussa P25	0.61	14.9	0.52	4.73
TiO_2	0.70	14.33	0.51	4.90
TiO_2−MWCNT	0.70	21.9	0.49	7.37

within the nanostructured TiO_2 film [which directly increases the short-circuit current (J_{SC})] are regarded as the two most important factors controlling the overall IPCE of the cell. Enhancement in the photoconversion efficiency in the present experiments suggests that charge collection and transport in these films are considerably improved by incorporating MWCNTs in the network in the form of integrated nanocomposites.

The cell performances of the DSSCs based on the MWCNT−TiO_2 nanocomposite electrodes were measured under 1 sun AM 1.5 simulated sunlight with an active area of 0.25 cm^2. Figure 7 and Table 1 compare the $J-V$ characteristics for DSSCs prepared with the nanocomposite electrodes (MWCNT 0.2 wt %), TiO_2 NPs, and P25. It can be seen that for the case of the nanocomposite, J_{SC} is about 22 mA/cm^2, which is almost 47% higher than that for P25 and 53% higher than that for TiO_2 NPs. The open-circuit voltage (V_{oc}) is 0.70 V (same as that compared to TiO_2 NPs) and 0.61 V for P25. As a result, the energy conversion efficiency of the cells made from our nanocomposite is 56% higher

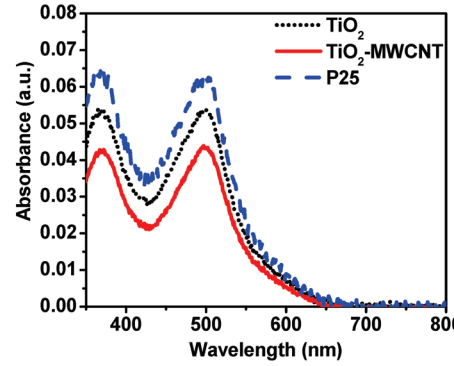

FIGURE 8. Absorptions of solutions containing dye detached from the TiO_2 (short dotted line), TiO_2−MWCNT nanocomposite (solid line), and P25 (dashed line) films (all with 1 cm^2 area) in 10 mL of H_2O with 1 mM KOH.

(=7.37%) than that for P25 (=4.73%) and 51% higher than that for TiO_2 NPs (=4.9%). It is useful to mention here that the weight percent of MWCNT, for which the results are given here, is roughly near optimum from the standpoint of efficiency. The efficiency was seen to fall by almost a factor of 2 upon increasing the weight percent of MWCNT to 0.5% (presumably because of the adverse dye loading effect discussed later). A plot of the power conversion efficiency as a function of the MWCNT concentration has been given in Figure SI-1 in the Supporting Information.

Figure 8 shows absorptions of solutions containing dye detached from the TiO_2 (short dotted line), TiO_2−MWCNT nanocomposite (solid line), and P25 (dashed line) films (all with 1 cm^2 area) in 10 mL of H_2O with 1 mM KOH. We can calculate from Figure 8 the dye loadings of the P25, TiO_2, and TiO_2−MWCNT nanocomposite films, which are 4.5×10^{-8}, 4.1×10^{-8}, and 3.37×10^{-8} mol/cm^2, respectively. It is interesting that, although the dye loading of the TiO_2−MWCNT nanocomposite is less as compared to P25 and TiO_2 NPs, the energy conversion efficiency of the cells made from the nanocomposite is higher than both. This can be attributed to an improved charge-carrier transport afforded by MWCNT and possibly a lower recombination as well. We believe that the effective molecular and thereby electronic coupling realized in our hydrothermal synthesis process is responsible for the significant enhancement of the conversion efficiency.

CONCLUSIONS

In conclusion, high (~7.4%) conversion efficiency is realized in DSSCs based on a hydrothermally synthesized TiO_2−MWCNT nanocomposite. This represents a ~50% improvement vis-a-vis cells made with hydrothermally synthesized TiO_2 without MWCNT or Degussa P25 powder. FT-IR data suggest that the −COOH groups open up on the surface of MWCNT under hydrothermal processing conditions and these conjugate with the Ti precursor to yield a composite. This integral conjugation appears to be effective in the charge-transfer process. Although MWCNT appears to reduce dye loading to some extent, the efficient charge transfer from TiO_2 to MWCNT and the efficient electron transport by the latter appears to help to improve the efficiency by 50%.

Acknowledgment. The authors from NCL, Pune, India, gratefully acknowledge funding for this work by the Department of Information Technology (Dr. K. Kumar and Dr. S. Chatterjee), Government of India. Support under the DST nanoscience program is also gratefully acknowledged. This research was also supported by Nano R & D program through the National Research Foundation of Korea funded by the Ministry of Education, Science and Technology (2009-008-3214).

Supporting Information Available: Plot of the power conversion efficiency as a function of the MWCNT concentration. This material is available free of charge via the Internet at http://pubs.acs.org.

REFERENCES AND NOTES

(1) O'Regan, B.; Gratzel, M. *Nature* **1991**, *23*, 737–740.
(2) Grätzel, M. *J. Photochem. Photobiol., C* **2003**, *4*, 145–153.
(3) Zhang, Q.; Chou, T.; Russo, B.; Jenekhe, S.; Cao, G. *Angew. Chem., Int. Ed.* **2008**, *47*, 2402–2406.
(4) Koo, H.; Kim, Y.; Lee, Y.; Lee, W.; Kim, K.; Park, N. *Adv. Mater.* **2008**, *20*, 195–199.
(5) Cameron, P. J.; Peter, L. M. *J. Phys. Chem. B* **2003**, *107*, 14394–14400.
(6) Xia, J.; Masaki, N.; Jiang, K.; Wada, Y.; Yanagida, S. *Chem. Lett.* **2006**, *35*, 252–253.
(7) Xia, J.; Masaki, N.; Jiang, K.; Yanagida, S. *Chem. Commun.* **2007**, 138–140.
(8) Palomares, E.; Clifford, J. N.; Haque, S. A.; Lutz, T.; Durrant, J. R. *J. Am. Chem. Soc.* **2003**, *125*, 475–482.
(9) Clifford, J. N.; Palomares, E.; Nazeeruddin, M. K.; Thampi, R.; Grätzel, M.; Durrant, J. R. *J. Am. Chem. Soc.* **2004**, *126*, 5670–5671.
(10) Park, N.-G.; Schlichthörl, G.; van de Lagemaat, J.; Cheong, H. M.; Mascarenhas, A.; Frank, A. J. *J. Phys. Chem. B* **1999**, *103*, 3308–3314.
(11) Sommmeling, P. M.; O'Regan, B. C.; Haswell, R. R.; Smit, H. J. P.; Bakker, N. J.; Smits, J. J. T.; Kroon, J. M.; van Roosmalen, J. A. M. *J. Phys. Chem. B* **2006**, *110*, 19191–19197.
(12) Wang, Z. S.; Kawauchi, H.; Kashima, T.; Arakawa, H. *Coord. Chem. Rev.* **2004**, *248*, 1381–1389.
(13) Ito, S.; Zakeerudiin, S. M.; Humphry-Baker, R.; Liska, P.; Charvet, P.; Comte, P.; Nazeeruddin, M. K.; Péchy, P.; Takata, M.; Miura, H.; Uchida, S.; Grätzel, M. *Adv. Mater.* **2006**, *18*, 1202–1205.
(14) Hore, S.; Vetter, C.; Kern, R.; Smit, H.; Hinsch, A. *Sol. Energy Mater. Sol. Cells* **2006**, *90*, 1176–1188.
(15) Jiang, C.; Sun, X.; Ko, G.; Kwong, D.; Wang, J. *Appl. Phys. Lett.* **2007**, *90*, 263501/1–3.
(16) Mor, G.; Varghese, O.; Paulose, M.; Shankar, K.; Grimes, C. *Sol. Energy Mater. Sol. Cells* **2006**, *90*, 2011–2075.
(17) Kongkanand, A.; Domıńguez, R.; Kamat, P. *Nano Lett.* **2007**, *7*, 676–680.
(18) Brown, P.; Takechi, K.; Kamat, P. *J. Phys. Chem. C* **2008**, *112*, 4776–4782, and references cited therein.
(19) Kongkanand, A.; Kamat, P. *ACS Nano* **2007**, *1*, 13–21.
(20) Jang, S.; Vittal, R.; Kim, K. *Langmuir* **2004**, *20*, 9807–9810.
(21) Yen, C.; Lin, Y.; Liao, S.; Weng, C.; Huang, C.; Hsiao, Y.; Ma, C.; Chang, M.; Shao, H.; Tsai, M.; Hsieh, C.; Tsai, C.; Weng, F. *Nanotechnology* **2008**, *19*, 1–9.
(22) Kim, S.; Jang, S.; Vittal, R.; Lee, J.; Kim, K. *J. Appl. Electrochem.* **2006**, *36*, 1433–1439.
(23) Lee, K.; Hu, C.; Chen, H.; Ho, K. *Sol. Energy Mater. Sol. Cells* **2008**, *92*, 1628–1633.
(24) Lee, T.; Alegaonkar, P.; Yoo, J. *Thin Solid Films* **2007**, *515*, 5131–5135.
(25) Zhu, Y.; Elim, H.; Foo, Y.; Yu, T.; Liu, Y.; Ji, W.; Lee, J.; Shen, Z; Wee, A.; Thong, J.; Sow, C. *Adv. Mater.* **2006**, *18*, 587–592.
(26) Vietmeyer, F.; Seger, B.; Kamat, P. *Adv. Mater.* **2007**, *19*, 2935–2940.
(27) Yan, X.; Tay, B.; Yang, Y.; Yung, W. *J. Phys. Chem. C* **2007**, *111*, 17254–17259.
(28) Chen, L.; Zhang, B.; Qu, M.; Yu, Z. *Powder Technol.* **2005**, *154*, 70–72.
(29) Sawatsuk, T.; Chindaduang, A.; Sae-kung, C.; Pratontep, S.; Tumcharern, G. *Diamond Relat. Mater.* **2009**, *18*, 524–527.
(30) Byrappa, K.; Adschiri, T. *Prog. Cryst. Growth Charact. Mater.* **2007**, *53*, 117–166.
(31) Beusen, J.; Van Bael, M.; Van den Rul, H.; D'Haen, J.; Mullens, J. *J. Eur. Ceram. Soc.* **2007**, *27*, 4529–4535.
(32) Choi, H.; Jung, Y.; Kim, S. *Bull. Korean Chem. Soc.* **2004**, *25*, 426–428.
(33) Zhu, Y.; Izaac Elim, H.; Foo, Y.; Yu, T.; Liu, Y.; Ji, W.; Lee, J. Y.; Shen, Z.; Wee, A. T. S.; Thong, J. T. L.; Sow, C. H. *Adv. Mater.* **2006**, *18*, 587–592.
(34) Xu, C.; Zhang, P.; Yan, L. *J. Raman Spectrosc.* **2001**, *32*, 862–865.
(35) Silverstein, R. M.; Bassler, G. C.; Morrill, T. C. *Spectroscopic Identification of Organic Compounds*, 3rd ed.; John Wiley and Sons: New York, 1974.

AM900396M